Evolution of low-frequency quasi-periodic oscillations in GX 339-4 during its 2021 outburst using *AstroSat* data

Santanu Mondal [1]★ Anirudh Salgundi [1,2] Debjit Chatterjee [1] Arghajit Jana [3,4] H.-K. Chang [3] and Sachindra Naik [5]

[1] *Indian Institute of Astrophysics, II Block Koramangala, Bangalore 560034, India*
[2] *Indian Institute of Technology Bombay, Powai 400076, India*
[3] *Institute of Astronomy, National Tsing Hua University, Hsinchu 300044, Taiwan*
[4] *Instituto de Estudios Astrofísicos, Universidad Diego Portales, Av. Ejército Libertador 441, 8370191 Santiago, Chile*
[5] *Astronomy and Astrophysics Division, Physical Research Laboratory, Navrangpura, Ahmedabad 380009, Gujarat, India*

ABSTRACT

The black hole X-ray binary GX 339-4 showed an X-ray outburst during 2021. The *AstroSat* captured this outburst when the source entered into the intermediate flux state while the count rate was declining. The source showed an alternating flux profile in a time-scale of $\lesssim 100$ ks, where the hard energy band was more variable than the soft band. The energy-dependent timing study showed that the observed quasi-periodic oscillation (QPO) was prominent in the low-energy bands, with its nearly sub-harmonic and harmonic components. These components appear and disappear with time, as observed in the orbit-wise QPO study. The Q-value, fractional rms, and 4.8–5.6 Hz frequency infer the QPOs as type-B and the spectral state as soft intermediate. The rms spectra of all orbits exhibiting QPOs show an increase in amplitude till ~ 10 keV, beyond which it starts decreasing. This may indicate that ~ 10 keV photons contributed relatively more in QPOs than other energy band photons. The Lorentzian normalization of the type-B QPO in different energy bands is consistent with the 10 keV peak. The energy-dependent time lag is complex and could be associated with the Comptonizing corona or jet. Finally, we discuss possible reasons behind the origin of different timing properties observed.

Key words: accretion, accretion discs – black hole physics – X-rays: binaries – X-rays: individual: GX 339-4.

1 INTRODUCTION

A transient black hole X-ray binary (BHXB) spends most of its time in quiescence and occasionally shows X-ray outbursts. During the outburst, the BHXBs show rapid variabilities in both spectral and temporal properties. The X-ray spectrum of a BHXB can be modelled by a multicolour disc blackbody (MCD) and a power-law tail (PL). The MCD is believed to arise from a geometrically thin and optically thick accretion disc (Shakura & Sunyaev 1973), while the PL tail is believed to originate from a hot electron cloud known as Compton cloud or corona (e.g. Haardt & Maraschi 1993; Chakrabarti & Titarchuk 1995; Done, Gierliński & Kubota 2007). The soft thermal photons emerging from the disc undergo inverse-Compton scattering in the Compton cloud, producing a hard Comptonized PL tail (Sunyaev & Titarchuk 1980, 1985).

The fast variability is observed in the power-density spectra (PDS) of the light curve. The band-limited noise with a flat profile in $\nu - P_\nu$ space with a break frequency (ν_b) characterize the PDS (e.g. van der Klis 1989, 1994). The noise profile of the PDS can be approximated by one or more Lorentzian functions (e.g. Nowak et al. 2001; Belloni et al. 2005). Often, a peaked-noise or quasi-periodic oscillation (QPO) is seen in the PDS of the BHXBs. The low-frequency QPO (LFQPO; $\nu_{QPO} = 0.1-30$ Hz) can be classified as type-A, type-B, or type-C, depending on the Q-value ($Q = \nu/\Delta\nu$, ν and $\Delta\nu$ are the centroid frequency and full width half-maximum, FWHM), amplitude (per cent rms), and ν (see Casella, Belloni & Stella 2005, and references therein).

The correlation between the spectral and timing properties are observed in the hardness–intensity diagram (HID; e.g. Homan et al. 2001), accretion rate ratio–intensity diagram (ARRID; Mondal, Debnath & Chakrabarti 2014; Jana et al. 2016), rms–intensity diagram (RID; Muñoz-Darias, Motta & Belloni 2011), or hardness ratio–rms diagram (HRD; Belloni et al. 2005). An outbursting BHXB exhibits different spectral states during the outburst, which is seen in the different branches of the HID, ARRID, RID, or HRD. Generally, the BHXB goes through low–hard state (LHS), hard–intermediate state (HIMS), soft–intermediate state (SIMS), and high–soft state (HSS) during the outburst (e.g. Remillard & McClintock 2006; Nandi et al. 2012; Jana 2022). A detailed study on the spectral state evolution has been made by several groups for different outbursting BHXBs (e.g. Remillard & McClintock 2006; Chatterjee et al. 2016).

The physical mechanism of LFQPO is not well-understood. Several models have been proposed to explain the origin of the LFQPO in BHXBs, including magneto-acoustic waves (e.g. Titarchuk, Lapidus & Muslimov 1998; Cabanac et al. 2010), spiral

★ E-mail: santanuicsp@gmail.com, santanu.mondal@iiap.res.in

density waves (e.g. Varnière & Tagger 2002; Varnière, Tagger & Rodriguez 2012), Lense–Thirring precession (e.g. Stella, Vietri & Morsink 1999; Ingram, Done & Fragile 2009), and shock oscillation model (e.g. Molteni, Sponholz & Chakrabarti 1996; Chakrabarti et al. 2005, 2008). Most models do not consider the spectral properties of the BHXBs while explaining the LFQPOs. However, one needs a general comprehensive model to explain both spectral and timing properties physically. The shock oscillation model is one such model that can explain both spectral and timing properties in a single framework (Chakrabarti, Mondal & Debnath 2015; Chatterjee et al. 2016).

Transient BHXB GX 339-4 went into an X-ray outburst in 2021 January that lasted for about 10 months (Corbel et al. 2021; Garcia et al. 2021). *AstroSat* observed the source for a total of 600 ks between 2021 March 30 and April 6 when the source was in the intermediate state. We studied the timing and spectral properties of the source in detail using the data from the *AstroSat* observations. We present the timing properties of GX 339-4 during the intermediate state in this paper. The spectral properties will be presented elsewhere. The paper is organized in the following way. In Section 2, the data reduction and analysis process are presented. In Section 3, we present the results of the temporal analysis. Finally, in Section 4, we discuss our results.

2 OBSERVATIONS AND DATA ANALYSIS

AstroSat (Singh et al. 2014; Agrawal et al. 2017) is India's first multiwavelength astronomical observatory, which contains five instruments on board: Soft X-ray Telescope (SXT), Large Area X-ray Proportional Counter (LAXPC), Cadmium Zinc Telluride Imager (CZTI), a Scanning Sky Monitor (SSM), and an Ultra-Violet Imaging Telescope (UVIT). Among them, the LAXPC is the ideal instrument to probe rapid time variability studies of X-ray binaries with moderate spectral capabilities. The high sensitivity and medium resolution spectral capability of SXT in the $0.3-8$ keV energy band are useful for broad-band spectral studies simultaneously with LAXPC. These capabilities provided a unique opportunity to investigate the spectro-timing properties of several X-ray binaries (including new transients), particularly BHXRBs using *AstroSat*.

LAXPC has three units such as LAXPC10, LAXPC20, and LAXPC30, operating in the $3-80$ keV energy band. The three units have a total effective area of ~ 6000 cm^2 in $5-20$ keV and record X-ray events with a time resolution of 10 μs (Yadav et al. 2016a, b; Agrawal et al. 2017; Antia et al. 2017). We used the Event Analysis (EA) mode data of the source and reduced the Level 1 data using the LAXPC software (LAXPCSOFT) to generate the Level 2 cleaned event files. Among the three units, LAXPC10 and LAXPC30 showed abnormal behaviours (gain change, low gain, and gas leakage). In addition, the LAXPC 30 has no longer been operational since 2018 March 8. Thus, for the present study, we have used the archival data of the *AstroSat* observations of GX 339-4 between 2021 March 30 and April 6 in the $3-80$ keV energy range from the LAXPC20 instrument. Further details of the observations are mentioned in Table 1.

The light curves were extracted using the task LAXPC_MAKE_LIGHTCURVE[1], and are background subtracted. The background estimation was done based on the blank sky observations, closest to the time of observation of the source (see Antia et al. 2017, for details). We divided the entire energy band ($3-30$ keV) combining all 74 orbits ($\sim$7 d) into several segments with narrow energy bands, namely $3-5.5$, $5.5-10$, $10-15$, $15-20$,

[1]*AstroSat* Science Support Cell: http://astrosat-ssc.iucaa.in/laxpcData

Table 1. Observation log of *AstroSat* data. In the second panel, only orbits ('O') that exhibit QPOs are mentioned.

Obs. ID	Start time MJD	Stop time MJD
T03_291T01_9000004278	59 303	59 310
O29750	59303.044	59303.091
O29755	59303.073	59303.178
O29756	59303.181	59303.516
O29758	59303.516	59303.564
O29759	59303.589	59303.637
O29760	59303.649	59303.742
O29761	59303.732	59303.815
O29763	59303.877	59303.961
O29764	59303.950	59304.033
O29765	59304.004	59304.106
O29770	59304.095	59304.318

and $20-30$ keV and generated PDS using LAXPC_REBIN_POWER task for each of them. As the background is dominated above 25 keV, we limited our PDS analysis up to 20 keV. We applied fast-Fourier transform (FFT) to the 0.01 sec time binned light curve. The light curves were divided into some intervals, where each interval consisted of 8192 bins. Then, we produced Poisson noise subtracted PDS for each of these segmented light curves and were averaged to make a single PDS for each observation. A geometrical rebinning with step 0.02 is used for generating PDS. Fractional rms is used to normalize all PDS. We have fitted the 5.5–10 keV band QPOs (see the next section) using multiple Lorentzian components and a power-law component: one with a narrow and strong component, which fits the fundamental QPO (ν_{qpo}^f), and the other two with relatively weaker components fitting the sub-harmonic (ν_{qpo}^s), harmonic (ν_{qpo}^h) QPOs, and the power-law component to model the broad-band noise. The power-law normalization of $2.96 \pm 0.39 \times 10^{-4}$ is measured.
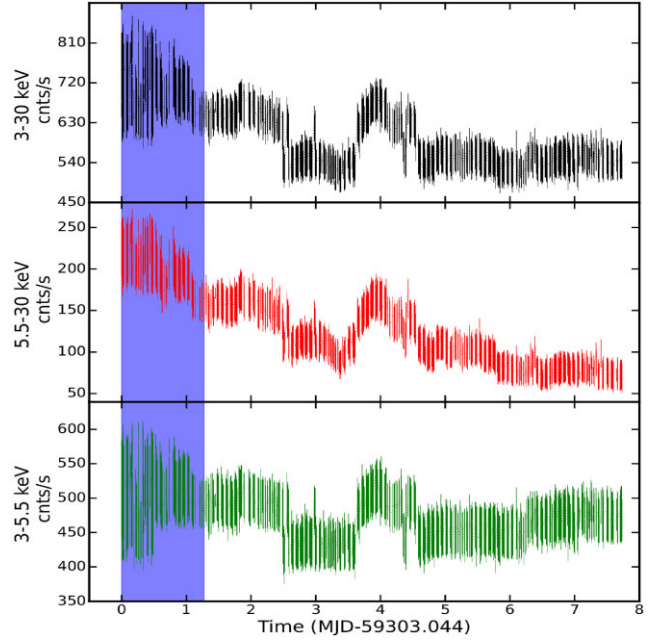
Further, we look for the evolution of ν_{qpo} during the *AstroSat* observation period. For that, we analysed data from each orbit separately and searched for QPOs. Out of 74 orbits, only 11 orbits showed the presence of QPOs with harmonic and sub-harmonic components. We fitted them using *Lorentzian* model and extracted the QPO parameters. The model fitted parameters for the 11 orbits are shown in Table 2. All uncertainties correspond to 90 per cent confidence level. We generally considered QPO if a peaked noise was detected at three sigma level. Besides the first 11 orbits, no peaked noise was observed in the PDS.

We estimated the energy-dependent time lag using LAXPC_FIND_FREQLAG for the combined 74 orbits. To generate the time-lag spectra, LAXPC subroutine provides inputs such as the frequency resolution (Δf) and frequency at which time lag has to be computed ($f = 5.06$ Hz in our case). The subroutine first generates PDS in different energy bands (between 3 and 32 keV with energy band size of 2 keV), with one of the bands set as reference (9–11 keV as the rms amplitude is maximum in this band). It then estimates the phase of the cross-correlation function for each energy band with the reference band. The time lag was calculated by dividing the phase lag by $2\pi f$. The detail description on time lag calculation (Nowak, Wilms & Dove 1999) and *LAXPC* subroutine can be found in Misra et al. (2017) and Husain et al. (2023, and references therein). The coherence factor varies between 0.1 and 3.5. To estimate the rms amplitude spectra, a 0.1–50 Hz frequency range is considered.

Table 2. Best-fitting QPO frequencies and their properties. The first 11 rows show the QPO properties of all 11 orbits when the QPOs are observed. The last panel shows the QPO properties in the 5.5–10 keV energy band when all 74 orbits (~7 d) are merged together.
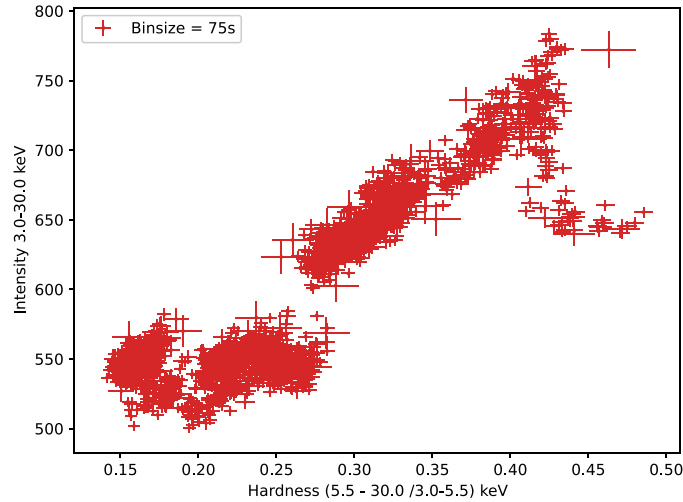
Orbit (X=297)	Cnt rate (Cnts s^{-1})	Funda. (ν_{qpo}^f Hz)	FWHM (Hz)	Norm (10^{-3})	Fractional rms (per cent)	Q	Harmonic (ν_{qpo}^h Hz)	FWHM (Hz)	Norm (10^{-4})	s-Harmonic (ν_{qpo}^s Hz)	FWHM (Hz)	Norm (10^{-3})
X50	720 ± 1	5.32 ± 0.02	0.72 ± 0.06	42 ± 2	0.81 ± 0.04	7.39 ± 0.62	–	–	–	2.28 ± 0.17	0.56 ± 0.30	7 ± 2
X55	720 ± 2	5.34 ± 0.01	0.79 ± 0.03	45 ± 1	0.88 ± 0.02	6.76 ± 0.26	–	–	–	2.77 ± 0.05	0.75 ± 0.13	11 ± 1
X56	685 ± 2	5.32 ± 0.02	1.00 ± 0.05	28 ± 1	0.80 ± 0.03	5.32 ± 0.27	–	–	–	2.80 ± 0.09	1.66 ± 0.14	30 ± 2
X58	722 ± 3	5.57 ± 0.02	1.02 ± 0.06	40 ± 2	0.94 ± 0.04	5.46 ± 0.32	–	–	–	2.80 ± 0.08	1.15 ± 0.24	18 ± 2
X59	710 ± 2	5.05 ± 0.01	0.56 ± 0.02	58 ± 2	0.85 ± 0.02	9.02 ± 0.32	10.08 ± 0.14	0.41 ± 0.38	10 ± 4	–	–	–
X60	689 ± 2	4.89 ± 0.01	0.45 ± 0.02	54 ± 1	0.74 ± 0.02	10.87 ± 0.48	–	–	–	–	–	–
X61	674 ± 2	4.75 ± 0.01	0.42 ± 0.02	49 ± 1	0.69 ± 0.02	11.31 ± 0.54	9.49 ± 0.36	0.12 ± 0.21	10 ± 2	–	–	–
X63	699 ± 2	4.89 ± 0.01	0.47 ± 0.02	54 ± 1	0.76 ± 0.02	10.40 ± 0.44	9.76 ± 0.06	0.40 ± 0.16	10 ± 3	–	–	–
X64	689 ± 1	4.80 ± 0.01	0.43 ± 0.02	53 ± 1	0.72 ± 0.02	11.16 ± 0.52	9.46 ± 0.06	0.18 ± 0.17	10 ± 2	–	–	–
X65	694 ± 1	4.86 ± 0.01	0.42 ± 0.02	54 ± 1	0.72 ± 0.02	11.57 ± 0.55	9.55 ± 0.09	0.36 ± 0.23	10 ± 3	–	–	–
X70	663 ± 2	4.83 ± 0.01	0.39 ± 0.02	19 ± 1	0.42 ± 0.02	12.38 ± 0.64	–	–	–	–	–	–
Merged 74 orbits	629 ± 1	5.06 ± 0.01	0.91 ± 0.03	70 ± 2	1.26 ± 0.03	5.56 ± 0.18	9.77 ± 0.19	2.50 ± 0.64	10 ± 3	2.14 ± 0.08	0.69 ± 0.26	50 ± 10

Figure 1. *AstroSat*/LAXPC20 light curves of GX 339-4 in different energy bands for all 74 orbits, from the top, 3.0−30.0 keV (top panel), 5.5−30.0 keV (middle panel), and 3.0−5.5 keV (bottom panel), respectively. The bottom panel shows the hardness ratio (5.5−30.0 keV/3.0−5.5 keV). The vertical shaded region shows the 11 orbits in which QPOs are observed. The '0' (zero) in the X-axis represents MJD = 59303.044.

3 RESULTS AND DISCUSSIONS

Fig. 1 shows the light curves of GX 339-4 in different energy bands during the observation period. From the top, the panels in Fig. 1 correspond to energy bands 3.0−30.0, 5.5−30.0, and 3.0−5.5 keV, respectively. In the hard band (5.5−30.0 keV), flux has changed by a factor of 2, whereas in the soft band (3.0−5.5 keV) flux change is by a factor of 1.2. These changes indicate that the hard flux is more variable than the soft flux, which is quite expected, as the hard radiations are coming from the inner hot region, where temperature and the size of the corona can change significantly due to the change in accretion flow parameters (Chakrabarti & Titarchuk 1995) in a time-scale of days. Alternatively, it has been observed that the change in rms-energy spectra in different spectral states can also be a probe to identify such flux changes, which may depend on the intrinsic variability of the corona (Belloni, Motta & Muñoz-Darias 2011). However, as we have short-term data, and it belongs to one spectral state only, verifying such a probe is beyond our scope. In addition, there is an alternating flux state (AFS; Liu et al. 2022) in all energy bands in the *Insight-HXMT* data for this source observed during 2021 April 1–2. The AFS looks similar to 'Flip-Flop' profile (FFP) as observed for other sources (Jithesh et al. 2019; Bogensberger et al. 2020, and references therein) including GX 339-4 (Miyamoto et al. 1991). This AFS (here, time-scale is ≲100 ks) might not be the same as the FFP in terms of their variability time-scale. It is possible that some outflows/jet activities were triggered during that time, and the flux went down, as outflows/jets can carry some energy and mass from the inner corona region. However, some other effects, e.g. the change in mass accretion rate due to change in viscosity (Lyubarskii 1997; Mondal et al. 2017) or irradiation (King & Ritter 1998; Mondal 2020a) can generate such fluctuations in the light curve. We note that either FFP, AFS, or X-ray variability in general in a short time
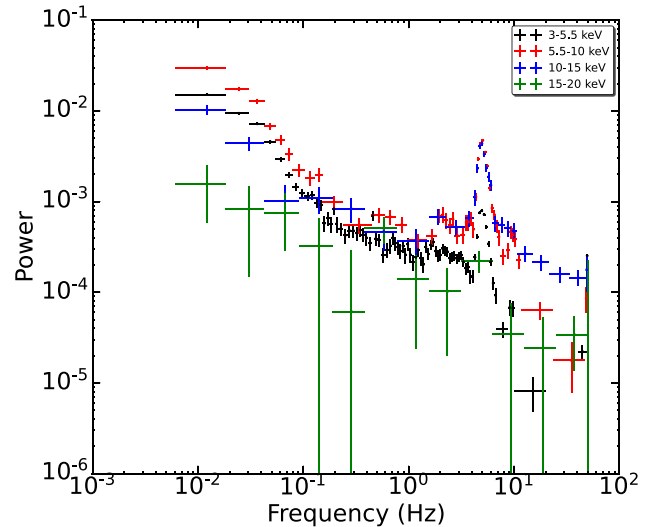
Figure 2. Hardness–intensity diagram is plotted during the *AstroSat* observation of the source. Based on the QPO properties including frequency, fractional rms, and Q-factor, the HID falls in the SIM branch of the full HID shown in Peirano et al. (2023).

interval can be explained due to the change in corona temperature and geometry, which are the effects of change in mass accretion rate (Mondal & Jithesh 2023, see for recent FFP study.). In a follow-up work Jana et al. (in preparation) are studying the spectra of all orbits to explain such X-ray variabilities of the source.

The HID during the *AstroSat* observation period is shown in Fig. 2. Based on the QPO properties including frequency, fractional rms, and quality factor (see also Motta et al. 2011; Belloni & Motta 2016), our estimated HID using *AstroSat* data falls in the SIM branch of the full HID, which has been shown by Peirano et al. (2023) using *NICER* data. In the later sections, we confirm that the spectral state is SIM state (SIMS) using different QPO properties. We should mention that the authors used a different energy band to calculate the hardness ratio. Therefore, some discrepancies between the HIDs may arise. This is expected as hardness has no standard reference energy bands and changes with the availability of energy bands in different instruments.
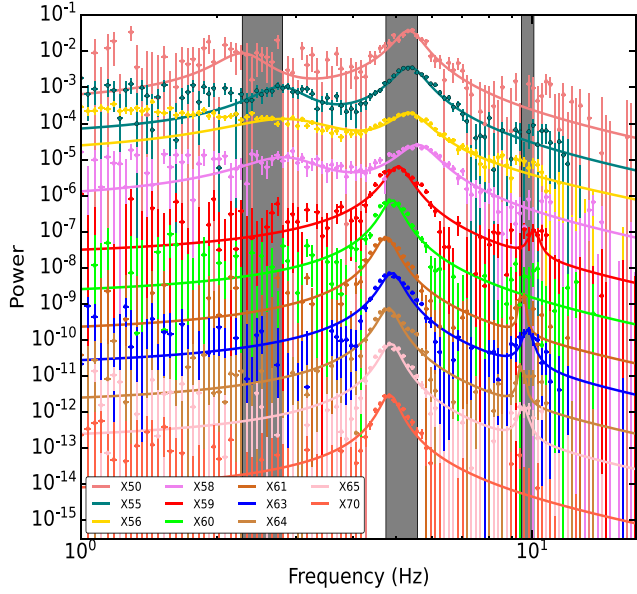
Along with the flux variability, the light curve variabilities become prominent when we look at the PDS of the same light curves. Fig. 3 shows the PDS in different energy bands. Interestingly, high energy bands (>20 keV) do not show any prominent QPOs, while in the low energy bands (<15 keV), sharp QPOs with harmonics and sub-harmonics are observed. The data above 20 keV are noisy, due to which QPOs were not detected in this energy range. However, it does not mean the QPOs are absent in the light curves beyond 20 keV. Jin et al. (2023) observed QPOs above 50 keV for this source in *Insight-HXMT* data and other sources also showed the presence of QPOs at higher energy bands (see Homan et al. 2001; Ma et al. 2021). The ν_{qpo} observed from the combined 74 orbits in the energy band 5.5–10 keV are 2.14 ± 0.08 ($\nu_{\mathrm{qpo}}^{\mathrm{s}}$), 5.06 ± 0.01 ($\nu_{\mathrm{qpo}}^{\mathrm{f}}$), and 9.77 ± 0.19 Hz ($\nu_{\mathrm{qpo}}^{\mathrm{h}}$). The other parameters of the QPOs fitting are shown in the bottom panel of Table 2. For the orbits 29 756 and 29758, $\nu_{\mathrm{qpo}}^{\mathrm{s}}$ and $\nu_{\mathrm{qpo}}^{\mathrm{f}}$ follow a 1:2 ratio. However, the other two orbits do not. While we merged all orbit data, the QPO frequencies approximately satisfy the 1:2 ratio. Very recently, similar QPO frequencies were reported by Peirano et al. (2023) for this source using *AstroSat* and *NICER* data. Authors used data of 7 orbits of *AstroSat* among 11 orbits that showed QPOs, and the inferred QPO properties and spectral type remained the same as we observed in this work.
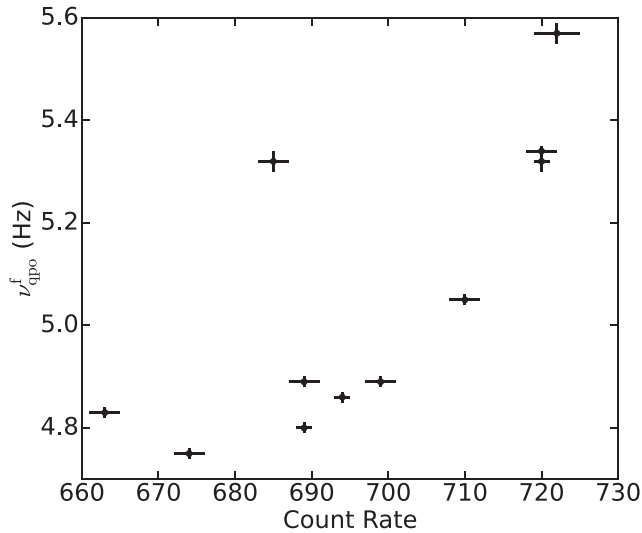

Figure 3. The power density spectra (PDS) of GX 339-4 for different energy bands. All PDS are merged, combining all 74 orbits. Multiple Lorenzian components and a power-law component are used to fit the QPOs. The lower panel of Table 2 shows the QPO frequency estimated for the merged orbits for the energy band 5.5–10 keV and the Lorentzian model components. The power-law model is used to fit the broad-band noise with normalization of $2.96 \pm 0.389 \times 10^{-4}$. A geometrical rebinning factor with step 0.02 is used for generating the PDS.

The orbit-wise (for 11 orbits) PDS fits are shown in Fig. 4 and the corresponding QPO parameters are given in Table 2. The data and their errors are presented with '+' symbol, and the same colour line represents the fitted Lorentzian models. The vertical shaded regions (grey) show the shift in peak frequencies for all three QPOs ($\nu_{\mathrm{qpo}}^{\mathrm{s}}$, $\nu_{\mathrm{qpo}}^{\mathrm{f}}$, $\nu_{\mathrm{qpo}}^{\mathrm{h}}$), respectively. Moreover, we estimated the fractional rms and Q-values of the frequencies for all 11 orbits. Our estimated fractional rms is between 0.4 per cent and 0.9 per cent and the $\nu_{\mathrm{qpo}}^{\mathrm{f}}$ varies between 4.8 and 5.6 Hz. A series of studies showed that the type-B QPOs are limited to the range of 1–6 Hz, but the detections during high-flux intervals are concentrated in the narrow 4–6 Hz range. The

Figure 4. Orbit-wise variation of QPOs in the 3–25 keV energy band. 'X' denotes the common prefix of orbit notation '297'. The power is scaled manually during plotting for visual clarity. The range of the sub-harmonic, fundamental, and harmonic peak frequencies are marked as vertical shared regions. The data values and errors are shown with '+' symbol, and the same colour line represents the model.

Figure 5. Fundamental QPO frequency increases with increasing count rate in the 3–25 keV energy band during the observation period.

centroid frequency appears positively correlated with source intensity rather than hardness (see Casella, Belloni & Stella 2005; Belloni, Motta & Muñoz-Darias 2011; Motta et al. 2011; Belloni & Motta 2016). If we compare our findings with the above classification, our data fall in the SIMS, and the QPO nature is type-B. Additionally, we have further checked the correlation between ν^f_{qpo} and intensity or count rate to compare with the above studies, which is shown in Fig. 5.

At the start of the observation, the sub-harmonic QPO appeared in a couple of orbits and then disappeared, but the harmonic was absent
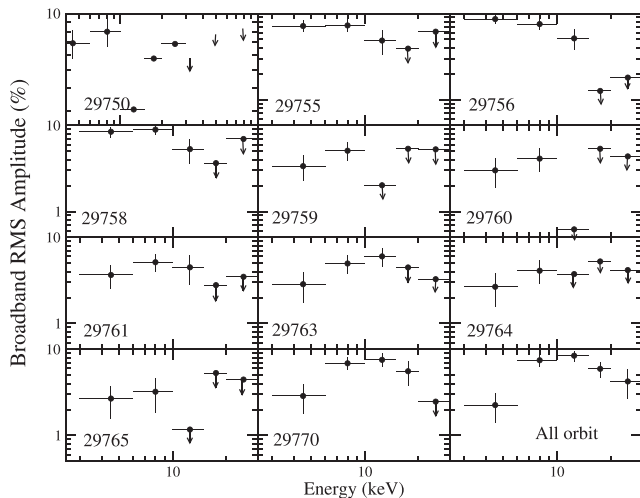
during that time. However, the opposite scenario was observed during the later time of the outburst. The appearance and disappearance of QPOs are intrinsic to the source, which can be due to the change in accretion flow parameters that are triggering such behaviour, or it can be due to the launching of jets/mass outflows from the system (see Fender, Belloni & Gallo 2004; Sriram, Rao & Choi 2016; Mondal & Jithesh 2023, and references therein). The QPOs are only observed in the first 11 orbits (MJD 59303.06–59304.20) of the *AstroSat* observation, while the AFS is seen on MJD 59305–59306. Hence, there is no relation between AFS and the evolution of QPOs in this case, in comparison with the observation by Bogensberger et al. (2020, in Swift J1658.2-4242).

The evolution of the QPO frequencies shows some interesting features, where either sub-harmonic or harmonic frequencies are present along with the fundamental. The evolution of QPOs and their harmonics can be explained using several popular models in the literature (see Ingram & Motta 2019, for a review). However, inferring the spectral state from QPO properties indicates that both spectral state and timing properties are interlinked. Therefore, the same model that explains the origin of QPOs should be able to fit the spectra. Such a physical connection between the spectral and timing properties is unlikely for the models discussed in the review. Therefore, it is suggestive and worth considering models which can explain both properties together. This motivates us to explain the evolution of the fundamental QPO frequency using the Propagating Oscillatory Shock model (POS; Chakrabarti et al. 2008; Nandi et al. 2012; Jana et al. 2016) including GX 339-4 (Debnath, Mondal & Chakrabarti 2015, and references therein), where an axisymmetric standing shock which is the boundary layer of the corona oscillates and produces such ν^f_{qpo}. The same shock that produces QPOs also decides spectral states during the outburst period of BHXRBs. In progressive days, as the source moves from a hard to soft state, the Keplerian disc moves inwards, and the cooling rate increases due to more soft photons getting scattered by the hot corona. Therefore, the corona shrinks, and QPO frequency increases. The electron number density and the temperature of the corona determine the cooling rate. However, explaining the harmonic or sub-harmonic frequencies requires some additional mechanisms, which can either be some perturbations to the axisymmetric shock and make it non-axisymmetric or the presence of more than one shock (Chakrabarti, Acharyya & Molteni 2004). As the source is observed in SIMS, it is clear that the dynamic corona or the centrifugal barrier has not completely disappeared, rather it moved inward due to an increase in mass accretion rate. In such a situation, one shock can break into fragments and oscillate in different frequencies (see Chakrabarti et al. 2009, for a review). On the other hand, turbulence can produce a second shock along with the centrifugal barrier. As GX 339-4 is a rapidly spinning black hole, and the turbulence has significant effects in originating LFQPOs (Mondal 2020b), it can be possible that two shocks oscillated in different frequencies and produced observed sub-harmonic or harmonic frequencies. However, performing numerical simulations in 3D can help in understanding such effects.

The QPOs and their evolution are directly linked with the size of the Comptonizing corona, whereas the time lag estimation not only gives the dynamic and thermodynamic properties of those regions but also about the energy-dependent physical processes that are responsible for the emission of photons from various regions of the disc (see, Cui et al. 1997; Nowak, Wilms & Dove 1999; Dutta & Chakrabarti 2016, and references therein). In one of the frameworks of the Comptonization process, soft radiations get up-scattered by the hot electron cloud and reach the observer later than the soft photons, which are directly coming to the observer. In Fig. 6, we show the

Figure 6. The energy dependent time lag estimated during the *AstroSat* observation period, considering ν_{qpo}^{f} as the centroid frequency of the source. During estimating the lag at the frequency 5.06 Hz, we used a frequency range of 3–7 Hz.

Figure 7. The rms spectra for all orbits when QPO is observed. Down arrow indicate the upper limit. The bottom right corner plot shows the rms amplitude for all 74 merged orbits. The rms amplitude values are estimated in the frequency range of 0.1–50 Hz.

energy-dependent time lag spectrum of the type-B QPO of GX 339-4. We find that the time lag is initially negative and increases with energy till ∼22 keV and then again negative. A similar lag behaviour was observed for this source by Jin et al. (2023). The positive lag attributes to the Comptonization, while the negative lag may be explained by the jet or outflow (Patra et al. 2019). Such complex behaviour of the lag spectrum may not be explained by a single mechanism such as viscosity fluctuation or the Comptonization process, it requires a detailed study using more broad-band data.

Fig. 7 shows the rms spectra for each orbit when the QPO is observed. For each 11 orbit (that showed QPOs), we observed that the rms rises slowly, reaches maximum ∼10 keV, and then decreases. Therefore, it is reasonable to say that the photons having energy ∼10 keV may contribute mostly to the QPOs (van der Klis 1989,

1994), suggesting that the coronal emission is responsible for the QPOs. To further cross-check this finding, we have fitted the QPO in Fig. 3 for different energy bands and noticed that Lorentzian normalization peaked for 5.5–10 keV band with values for all four bands are $(1.1, 6.9, 6.1, 4.0) \times 10^{-3}$ respectively. This is in accord with other BHXBs where rms peak is observed ∼10 keV (e.g. Alabarta et al. 2020; Jana et al. 2022). Interestingly, in the case of a neutron star, the peak is observed at higher energy (>20 keV; e.g. Wang, Chang & Liu 2012).

4 SUMMARY

During the 2021 outburst of GX 339-4, we found that the source showed significant variability in flux in a time-scale of ≲100 ks. A detailed energy-dependent temporal study using *AstroSat* data shows that:

(i) The source showed AFS in both hard and soft energy bands. However, the hard energy band is found to be more variable than the soft band. The AFS can originate due to the jet/mass outflow activity or some local viscosity fluctuations in the disc.

(ii) The soft energy band showed more prominent QPO along with its sub-harmonic and harmonic frequencies. In the hard energy bands, however, the QPO peaks become broader, and its components disappear. This can be due to a low S/N ratio in the data and may present in high-energy bands as well.

(iii) Orbit-wise QPO study shows that the QPO frequency evolves with time. The sub-harmonics appear during the start of the observation and disappear at a later time, while the opposite scenario was observed for the harmonics.

(iv) The evolution of QPO frequencies indicates that the size of the Comptonizing corona evolved with time, in agreement with the propagating oscillatory shock and multiple-shock scenario.

(v) The energy-dependent time lag study infers its association and origin from the Comptonizing corona. In our study, we found both positive and negative lag, whose origin can not be explained only using the Comptonization process. Some other complex processes might be responsible. To understand that, more broad-band data is required to be analysed.

(vi) In the rms spectra, the rms is observed to peak around ∼10 keV, suggesting that mostly photons with energy ∼10 keV are responsible for the QPOs.

DATA AVAILABILITY

The data used in this article are available in the ISRO's Science Data Archive for *AstroSat* Mission (https://astrobrowse.issdc.gov.in /astro_archive/archive/Home.jsp). The analysis techniques used in

the paper can be shared on reasonable request to the corresponding author.

REFERENCES

Agrawal P. C. et al., 2017, J. Astrophys. Astron., 38, 30
Alabarta K. et al., 2020, MNRAS, 497, 3896
Antia H. M. et al., 2017, ApJS, 231, 10
Belloni T., Homan J., Casella P., van der Klis M., Nespoli E., Lewin W. H. G., Miller J. M., Méndez M., 2005, A&A, 440, 207
Belloni T. M., Motta S. E., 2016, in Bambi C., ed., Astrophysics and Space Science Library Vol. 440, Astrophysics of Black Holes: From Fundamental Aspects to Latest Developments. Springer-Verlag, Berlin, p. 61
Belloni T. M., Motta S. E., Muñoz-Darias T., 2011, Bull. Astron. Soc. India, 39, 409
Bogensberger D. et al., 2020, A&A, 641, A101
Cabanac C., Henri G., Petrucci P. O., Malzac J., Ferreira J., Belloni T. M., 2010, MNRAS, 404, 738
Casella P., Belloni T., Stella L., 2005, ApJ, 629, 403
Chakrabarti S., Titarchuk L. G., 1995, ApJ, 455, 623
Chakrabarti S. K., Acharyya K., Molteni D., 2004, A&A, 421, 1
Chakrabarti S. K., Nandi A., Debnath D., Sarkar R., Datta B. G., 2005, preprint (arXiv:astro-ph/0508024)
Chakrabarti S. K., Debnath D., Nandi A., Pal P. S., 2008, A&A, 489, L41
Chakrabarti S. K. et al., 2009, preprint (arXiv:0903.1482)
Chakrabarti S. K., Mondal S., Debnath D., 2015, MNRAS, 452, 3451
Chatterjee D., Debnath D., Chakrabarti S. K., Mondal S., Jana A., 2016, ApJ, 827, 88
Corbel S., Tzioumis T., Tremou L., Carotenuto F., 2021, ATel, 14953, 1
Cui W., Zhang S. N., Focke W., Swank J. H., 1997, ApJ, 484, 383
Debnath D., Mondal S., Chakrabarti S. K., 2015, MNRAS, 447, 1984
Done C., Gierliński M., Kubota A., 2007, A&A Rev., 15, 1
Dutta B. G., Chakrabarti S. K., 2016, ApJ, 828, 101
Fender R. P., Belloni T. M., Gallo E., 2004, MNRAS, 355, 1105
Garcia J., Tomsick J., Harrison F., Connors R., Mastroserio G., 2021, ATel, 14352, 1
Haardt F., Maraschi L., 1993, ApJ, 413, 507
Homan J., Wijnands R., van der Klis M., Belloni T., van Paradijs J., Klein-Wolt M., Fender R., Méndez M., 2001, ApJS, 132, 377
Husain N., Garg A., Misra R., Sen S., 2023, MNRAS, 525, 4515
Ingram A., Done C., Fragile P. C., 2009, MNRAS, 397, L101
Ingram A. R., Motta S. E., 2019, New A Rev., 85, 101524
Jana A., 2022, MNRAS, 517, 3588
Jana A., Debnath D., Chakrabarti S. K., Mondal S., Molla A. A., 2016, ApJ, 819, 107
Jana A., Naik S., Jaisawal G. K., Chhotaray B., Kumari N., Gupta S., 2022, MNRAS, 511, 3922
Jin Y. J., Wang W., Chen X., Tian P. F., Liu Q., Zhang P., Wu H. J., Sai N., 2023, ApJ, 953, 33
Jithesh V., Maqbool B., Misra R., T A. R., Mall G., James M., 2019, ApJ, 887, 101
King A. R., Ritter H., 1998, MNRAS, 293, L42
Liu H., Jiang J., Zhang Z., Bambi C., Ji L., Kong L., Zhang S., 2022, MNRAS, 513, 4308
Lyubarskii Y. E., 1997, MNRAS, 292, 679
Ma X. et al., 2021, Nat. Astron., 5, 94
Misra R. et al., 2017, ApJ, 835, 195
Miyamoto S., Kimura K., Kitamoto S., Dotani T., Ebisawa K., 1991, ApJ, 383, 784
Molteni D., Sponholz H., Chakrabarti S. K., 1996, ApJ, 457, 805
Mondal S., 2020a, Adv. Space Res., 65, 693
Mondal S., 2020b, MNRAS, 492, 804
Mondal S., Jithesh V., 2023, MNRAS, 522, 2065
Mondal S., Debnath D., Chakrabarti S. K., 2014, ApJ, 786, 4
Mondal S., Chakrabarti S. K., Nagarkoti S., Arévalo P., 2017, ApJ, 850, 47
Motta S., Muñoz-Darias T., Casella P., Belloni T., Homan J., 2011, MNRAS, 418, 2292
Muñoz-Darias T., Motta S., Belloni T. M., 2011, MNRAS, 410, 679
Nandi A., Debnath D., Mandal S., Chakrabarti S. K., 2012, A&A, 542, A56
Nowak M. A., Wilms J., Dove J. B., 1999, ApJ, 517, 355
Nowak M. A., Wilms J., Heindl W. A., Pottschmidt K., Dove J. B., Begelman M. C., 2001, MNRAS, 320, 316
Patra D., Chatterjee A., Dutta B. G., Chakrabarti S. K., Nandi P., 2019, ApJ, 886, 137
Peirano V., Méndez M., García F., Belloni T., 2023, MNRAS, 519, 1336
Remillard R. A., McClintock J. E., 2006, ARA&A, 44, 49
Shakura N. I., Sunyaev R. A., 1973, A&A, 24, 337
Singh K. P. et al., 2014, in Takahashi T., den Herder J.-W. A., Bautz M., eds, Proc. SPIE Conf. Ser. Vol. 9144, Space Telescopes and Instrumentation 2014: Ultraviolet to Gamma Ray. SPIE, Bellingham, p.91441S
Sriram K., Rao A. R., Choi C. S., 2016, ApJ, 823, 67
Stella L., Vietri M., Morsink S. M., 1999, ApJ, 524, L63
Sunyaev R. A., Titarchuk L. G., 1980, A&A, 86, 121
Sunyaev R. A., Titarchuk L. G., 1985, A&A, 143, 374
Titarchuk L., Lapidus I., Muslimov A., 1998, ApJ, 499, 315
van der Klis M., 1989, ARA&A, 27, 517
van der Klis M., 1994, ApJS, 92, 511
Varnière P., Tagger M., 2002, A&A, 394, 329
Varnière P., Tagger M., Rodriguez J., 2012, A&A, 545, A40
Wang J., Chang H. K., Liu C. Y., 2012, A&A, 547, A74
Yadav J. S. et al., 2016a, ApJ, 833, 27
Yadav J. S. et al., 2016b, in den Herder J.-W. A., Takahashi T., Bautz M., eds, Proc. SPIE Conf. Ser. Vol. 9905, Space Telescopes and Instrumentation 2016: Ultraviolet to Gamma Ray. SPIE, Bellingham, p. 99051D

This paper has been typeset from a TEX/LATEX file prepared by the author.